On the Evolution and Stability of Finite-Amplitude Mountain Waves

T. L. CLARK[1]

Atmospheric Environment Service, Downsview, Ontario, Canada M3H 5T4

W. R. PELTIER[2]

Department of Physics, University of Toronto, Toronto, Ontario, Canada M5S 1A7

(Manuscript received 16 May 1977, in revised form 26 July 1977)

ABSTRACT

We describe a series of fixed Froude number numerical simulations of the generation of internal gravity waves by the flow of stably stratified fluid over an isolated obstacle. Upstream of the obstacle the parallel flow is shear free and the Brunt-Väisälä frequency is independent of height. Under these conditions the nonhydrostatic model which we employ does not support resonance modes. In this model the nonlinear lower boundary condition is treated via a general tensor transformation which maps the domain with an irregular lower boundary into a rectangle. We explore the characteristics of the wave field as a function of the aspect ratio of the topography and show that there exists a critical aspect ratio which, if exceeded, results in the generation of internal waves which are subject to a local convective instability. In the long time limit we compare the numerically determined wave drag, the vertical profile of Reynolds stress and the downslope wind amplification to the corresponding predictions of linear steady-state theory. In the limit of small aspect ratio the analytic and numerical results coincide; in particular the Eliassen-Palm theorem is recovered. In the unstable regime the drag on the obstacle increases drastically, the strength of the downslope flow is enhanced and the vertical profile of Reynolds stress is strongly divergent. We discuss the implications of these results to the understanding of certain characteristics of mountain waves in the atmosphere.

1. Introduction

The mechanism of internal wave generation by the flow of stably stratified fluid over an isolated obstacle is well known. Such motions are commonly known as "mountain waves" on account of their common atmospheric occurrence, and a considerable theoretical and experimental effort has been directed toward the elucidation of their properties. Topographically induced internal waves are also a prevalent feature of the oceanic interior. Early work on their description included the contributions of Queney (1941), Lyra (1943) and Scorer (1949) in which linear theory was successfully exploited in explanation of various characteristics of the wave spectrum.

Sawyer (1959) was the first to elaborate upon the relative importance of the surface drag associated with the freely propagating component of the spectrum compared with the direct frictional drag in high Reynolds number geophysical flows. In the atmospheric context his calculations predicted typical surface stresses on the order of 1–10 dyn cm^{-2} in conjunction with stationary waves having horizontal wavelengths in the range 10–100 km. This estimate from linear theory was later

confirmed by Blumen (1965) who extended Sawyer's calculation to include three-dimensional and random effects of topography and vertical variations of mean flow speed and stability. Bretherton (1969) applied linear theory in a calculation of the wave drag which should be produced by a particular air flow over a specific geographical locality and again obtained a result in accord with Sawyer's estimate.

Though highly suggestive of the importance of mountain wave drag in the natural environment, this work could not be regarded as conclusive since it was entirely founded upon the predictions of linear theory. Conclusive verification was provided by Lilly (1972) in the description of a lee wave experiment conducted over the Rocky Mountains. He reported that "From aircraft traverses through moderate amplitude waves in the Front Range we have commonly obtained direct stress measurements of between 5 and 10 dyn cm^{-2} in the troposphere averaged over horizontal distances of 100–200 km." A detailed analysis of a particular set of data from this experiment was presented by Lilly and Kennedy (1973). A common characteristic of these observations of Reynolds stress in the wave field and those described elsewhere (e.g., Lilly and Zipser, 1972) is that although the vertical profile of horizontally averaged stress is reasonably uniform throughout most of the troposphere, in the upper troposphere and lower

stratosphere its magnitude decreases rapidly to zero. In this region the turbulence intensity is extreme.

Linear steady-state theory makes a very specific prediction regarding the nature of the vertical Reynolds stress profile which is embodied in the Eliassen-Palm theorem (Eliassen and Palm, 1960). If the wave amplitude is sufficiently small then the vertical divergence of the Reynolds stress is identically zero unless the mean horizontal flow reverses direction somewhere aloft. At such a critical level, Booker and Bretherton (1967), following Miles (1961), have shown that the wave amplitude is reduced by the factor

$$\exp[-2\pi(\mathrm{Ri}-\tfrac{1}{4})^{\frac{1}{2}}],$$

where Ri is the gradient Richardson number at the critical level and $\mathrm{Ri} > 0.25$ is assumed. For $\mathrm{Ri} > O(1)$ there is no significant reflection, and the momentum flux is thus entirely absorbed. The mean flow at this level is then subject to the full wave drag and will be decelerated by it. Breeding (1971) has simulated the ensuing nonlinear interaction and shown that the critical level migrates downward in response to the wave drag for horizontally periodic plane wave forcing from below.

If, on the other hand, $\mathrm{Ri} < 0.25$ at the critical level then not only is the flow dynamically unstable to the growth of Kelvin-Helmholtz waves (Miles, 1961; Howard, 1961), but any internal wave incident upon the critical level from below will be overreflected (Jones, 1968; Davis and Peltier, 1976; Acheson, 1976) and will thus amplify in time. Although both of these interactions lead to a vertical divergence of momentum flux, they both require the existence of a critical level. Such a level was not present in the observations reported by Lilly and Kennedy (1973) and thus the stress divergence associated with the standing wave structure is not explicable in linear theory.

Here we shall restrict our attention to those aspects of the mountain wave problem which are intrinsically dependent upon its nonlinearity. Such effects enter in two related ways, even when the turbulent boundary layer is excluded from consideration and a free-slip condition is applied at the surface. These nonlinearities are associated with 1) the lower boundary condition (e.g., the finite aspect ratio of the topography) and 2) the nonlinearity of the hydrodynamic equations themselves. Under restricted circumstances a limited amount of progress has been made in understanding these effects through the application of analytic methods (Miles, 1969; Long, 1972) but in general the problem is analytically intractable.

In Sections 2 to 5 we describe a finite-difference numerical model which has been designed explicitly to treat the fully nonlinear transient mountain wave problem. This model is based upon the anelastic form of the full Navier-Stokes equations and as such is a model from which sound waves have been filtered. It

has the following additional characteristics:

1) The physical domain with the irregular lower boundary is mapped into a parallelopiped (a rectangle for the two dimensional simulations described here) by a tensor transformation of the independent variables $(x,z) \rightarrow (\bar{x},\bar{z})$.

2) The conservative form is preserved by referring the dependent variables to the original Cartesian coordinates.

3) Effective numerical schemes are employed to simulate the Sommerfeld condition at lateral and overhead boundaries of the domain. These schemes effectively eliminate reflections.

In Section 6 we present a brief review of linear theory and apply it to calculate the steady-state wave field launched and maintained by a bell-shaped obstacle in a shear free flow which has constant Brunt-Väisälä frequency. This calculation is for a Froude number (ratio of launching frequency to Brunt-Väisälä frequency) such that the disturbance is freely propagating in the vertical. In Section 7 we employ the numerical model to analyze the transient development of the wave field and the approach to steady state as a function of the aspect (height/width) ratio of the obstacle. We compare these results in the long time limit to the predictions of linear steady-state theory and show that for small aspect ratios they are almost identical. For aspect ratios exceeding a critical value we show that the flow becomes unsteady and derive a linear stability criterion which explains the onset of unsteady behavior in terms of a convective instability of the wave field. The implications of our results to the geophysical observations described previously are discussed in Section 8.

2. The mathematical model

The model which we employ is based upon that described in numerical detail by Clark (1977) although it required some modification to obtain the results presented in Section 7. Its analytic structure is embodied in the anelastic form of the equations of motion, continuity and the first law of thermodynamics, respectively, as

$$\bar{\rho}\frac{d\mathbf{u}}{dt} = -\nabla p' + \nabla \cdot \tau + \rho' \mathbf{g}, \tag{1}$$

$$\nabla \cdot (\bar{\rho}\mathbf{u}) = 0, \tag{2}$$

$$\bar{\rho}\frac{d\theta}{dt} = \nabla \cdot \mathbf{H}, \tag{3}$$

where τ is the stress tensor, $\mathbf{H}$ the heat flux vector and θ the potential temperature to be defined below. In (1)-(3) the thermodynamic variables $\Psi = (\rho,p,T,\theta)$ have

been separated into two components as

$$\Psi = \bar{\Psi}(z) + \psi'(\mathbf{x}, t), \tag{4}$$

where the overbar denotes a background state which is in hydrostatic equilibrium and where ρ, p, T, θ are, respectively, the density, pressure, temperature and potential temperature of an ideal gas. Batchelor (1954) has shown that all wave frequencies above the Brunt-Väisälä frequency N, where

$$N^2 = \frac{g}{\bar{\theta}} \frac{d\bar{\theta}}{dz}, \tag{5}$$

are filtered when the local time rate of change of density is taken to vanish in the continuity equation. The above system is similar to that obtained in the Boussinesq limit since variations of density from the background profile are ignored except where they multiply the gravitational acceleration. In the simulations completed to date we have employed the so-called "deep equations" of Ogura and Philips (1962) since this system is exactly closed energetically. To obtain this closure it is necessary to assume that the background state is isentropic and this leads to the following expressions for the fields $\bar{\Psi}$:

$$\bar{\theta}(z) = \theta_0 \tag{6a}$$

$$\bar{T}(z) = \theta_0(1 - z/H_s) \tag{6b}$$

$$\bar{p}(z) = p_0(1 - z/H_s)^{1/\kappa} \tag{6c}$$

$$\bar{\rho}(z) = p_0(1 - z/H_s)^{1/(\kappa-1)} (R_d \theta_0)^{-1}. \tag{6d}$$

Since (6a) implies $N^2 = 0$ from (5) the model must be initialized at $t = 0$ with $\theta' = \theta'(z)$ in order that the medium be capable of supporting internal waves. In (6) p_0 is the pressure at $z = 0$, $\kappa = R_d/c_p$ and $H_s(= c_p\theta_0/g)$ is the isentropic scale height; R_d is the gas constant for dry air and c_p the specific heat capacity at constant pressure. In deriving (6) use has been made of the ideal gas equation of state

$$p = \rho R_d T, \tag{7}$$

the definition of potential temperature

$$\theta = T(p/p_0)^{-\kappa}, \tag{8}$$

and the condition for hydrostatic balance

$$\frac{dp}{dz} = -\rho g. \tag{9}$$

A linearization of (7) and (8) leads to the result

$$\rho' = -\bar{\rho}\frac{\theta'}{\bar{\theta}} + \frac{p'}{c^2}, \tag{10}$$

where $c^2 = \gamma R_d \bar{T}$ is the square of the adiabatic sound speed ($\gamma = C_p/C_v$). As stated previously, the advantage

of expansion about the state defined by (6) is that the resulting system (1)–(3) has a simple energy closure against which the numerical code may be easily checked. Such consistency experiments are described in detail in Clark (1977).

In (1) the symmetric stress tensor τ_{ij} is connected to the deformation tensor D_{ij} through the momentum diffusivity K_m (effective kinematic viscosity) such that

$$\tau_{ij} = \bar{\rho} K_m D_{ij}, \tag{11}$$

$$D_{ij} = \partial_j u_i + \partial_i u_j - 2 \frac{\delta_{ij}}{\delta_{ii}} \nabla \cdot \mathbf{u}. \tag{12}$$

We are obliged to allow for spatial and temporal variations of K_m in (11) for two reasons. The first of these is purely numerical. In order to suppress reflections from the upper lid of the domain and from the upstream boundary we have found it necessary to absorb the incident waves viscously. There is thus a requirement for high effective viscosity in these regions. Second, the geophysical flows in which we are interested have extremely high Reynolds number ($\gg 10^3$) and we require some way of accounting for the subgrid (unresolved) scale motions which may be engendered by instability of the resolved scales. We have tested the following formulations of the first-order closure schemes suggested by Lilly (1962):

$$K_m = (k\Delta)^2 | \text{Def} |, \tag{13a}$$

$$K_m = (k\Delta)^2 | \text{Def} | (1 - \text{Ri})^{\frac{1}{2}}, \quad \text{Ri} \lesssim 1, \tag{13b}$$

where

$$\text{Ri} = \frac{g(d \ln\theta/dz)}{(\text{Def})^2}, \tag{13c}$$

$$(\text{Def})^2 = \frac{1}{2}(D_{11}^2 + D_{22}^2) + D_{12}^2. \tag{13d}$$

Here and in what follows subscript 2 refers to the vertical coordinate. In (13) Δ is the grid resolution [$\Delta = (\Delta x \cdot \Delta z)^{\frac{1}{2}}$ in two dimensions] and k is a numerical constant. For three-dimensional simulations, Lilly (1967) found that $k = 0.21$ was consistent with the Kolmogoroff turbulence spectrum, and Deardorff (1971) showed that use of the form (13a) with $K_H/K_m = 1/\text{Pr} = 3$ (Pr = Prandtl number) and $k = 0.21$ was effective numerically in preventing spurious accumulation of energy at the 2Δ wavelength.

For all of the calculations to be described (13b) was assumed. In most cases this led to $K_m \equiv 0$ since Ri was everywhere greater than unity in the domain interior. Physically this assumption implies an instantaneous equilibration of the turbulence intensity with the large-scale flow in which it is embedded, an assumption which is not, in general, justifiable.

In (3) the heat flux vector $\mathbf{H}$ has components

$$H_i = \bar{\rho} K_H \frac{\partial \theta}{\partial x_i}, \tag{14}$$

and we shall always assume $K_H = K_m$ locally so that $\text{Pr} = 1$. Eqs. (1)–(3) and (10)–(14) complete the set of equations to be employed here.

An important analytic property of the system (1)–(3) is that the dependent variables u_i, θ', p' are not completely independent. The perturbation pressure field p', in particular, must be such that the velocity field computed from (1) satisfies the anelastic continuity equation (2) (Batchelor, 1954). The net result is that p' can no longer be determined from the equation of state (7) but rather must satisfy an elliptic partial differential equation which can be deduced by taking the divergence of (1) and applying (2). This equation is

$$(\bar\rho u_i u_j)_{,ji} = -(\delta_{ij} p')_{,ji} + (\delta_{i2}\rho' g)_{,i} + \tau_{ij,ji}, \qquad (15)$$

where $(\ )_{,i} = \partial(\ )/\partial x_i$. It is the necessity of solving this equation at each time step to update the pressure field which makes the anelastic system more difficult to work with numerically than the set of equations which obtain in the hydrostatic limit. In the next section these dynamical equations are transformed to a new coordinate system which depends upon the topography at the lower boundary.

3. Transformation of coordinates

In the two-dimensional version of the anelastic model employed here each of the four spatial boundaries of the domain require separate treatment. The lower boundary is particularly important in the mountain wave problem and we deal with it by transforming the hydrodynamic equations from (x,z) to $(\bar x,\bar z)$ coordinates where

$$\left.\begin{array}{l} \bar x = x \\[2mm] \bar z = H\dfrac{[z - z_s(x)]}{[H - z_s(x)]} \end{array}\right\}. \qquad (16)$$

This transformation has been employed previously by Gal-Chen and Somerville (1975a,b) who used it in a discussion of convection in air above a heated irregular boundary. The transformation (16) maps the domain

$$\left.\begin{array}{l} 0 \leqslant x \leqslant D \\[1mm] z_s(x) \leqslant z \leqslant H \end{array}\right\} \qquad (17)$$

into a rectangle. It becomes the identity transformation when the topography $z_s(x)$ vanishes and regardless of topography becomes the identity transformation at the top of the domain $z = H$. Furthermore, (16) is a 1:1 mapping between the old coordinates and the new since the Jacobian of the transformation

$$\sqrt{G} = 1 - z_s(x)/H \qquad (18)$$

is always nonzero. The conjugate of the metric tensor G_{mn} for the transformation (16) is the tensor G^{mn}, and

in the case of two spatial dimensions

$$G^{mn} = \begin{bmatrix} 1, & \dfrac{\partial z_s}{\partial x}\left(\dfrac{\bar z - H}{H - z_s(x)}\right) \\[4mm] \dfrac{\partial z_s}{\partial x}\left(\dfrac{\bar z - H}{H - z_s(x)}\right), & \left(\dfrac{\partial z_s}{\partial x}\right)^2\left(\dfrac{\bar z - H}{H - z_s}\right)^2 + \left(\dfrac{H}{H - z_s}\right)^2 \end{bmatrix}. \qquad (19)$$

If ϕ is an arbitrary field variable in the set of governing partial differential equations (1)–(3) then these equations may be transformed to the $(\bar x,\bar z)$ domain through application of the following expressions which obtain directly from the chain rule for partial derivatives:

$$\sqrt{G}\dfrac{\partial\phi}{\partial x}\bigg|_z = \dfrac{\partial}{\partial x}(\sqrt{G}\phi)\bigg|_{\bar z} + \dfrac{\partial}{\partial\bar z}(\sqrt{G}\,G^{12}\phi), \qquad (20a)$$

$$\sqrt{G}\dfrac{\partial\phi}{\partial z} = \dfrac{\partial\phi}{\partial\bar z}. \qquad (20b)$$

The complete transformation also requires the definition of fluid velocity normal to surfaces of constant $\bar z$ which we denote by ω, where

$$\omega = \dfrac{d\bar z}{dt} = (w + \sqrt{G}\,G^{12}u)/\sqrt{G}. \qquad (21)$$

In (21) u and w are, respectively, the x and z Cartesian components of fluid velocity. The analytic forms of the transformed equations are obtained by direct application of (20) and (21) to (1)–(3). They are as follows, respectively, for x and z momentum, continuity and the first law of thermodynamics:

$$\dfrac{\partial}{\partial t}(\bar\rho\sqrt{G}u) + \nabla\cdot(\Psi u)$$
$$= -\dfrac{\partial}{\partial x}(\sqrt{G}p') - \dfrac{\partial}{\partial\bar z}(\sqrt{G}\,G^{12}p')$$
$$+ \dfrac{\partial}{\partial x}(\sqrt{G}\tau_{11}) + \dfrac{\partial}{\partial\bar z}(\sqrt{G}\,G^{12}\tau_{11} + \tau_{12}), \qquad (22a)$$

$$\dfrac{\partial}{\partial t}(\bar\rho\sqrt{G}w) + \nabla\cdot(\Psi w)$$
$$= -\dfrac{\partial}{\partial\bar z}(p') - g\rho'\sqrt{G} + \dfrac{\partial}{\partial x}(\sqrt{G}\tau_{12})$$
$$+ \dfrac{\partial}{\partial\bar z}(\sqrt{G}\,G^{12}\tau_{12} + \tau_{22}). \qquad (22b)$$

$$\nabla\cdot(\Psi) = 0, \qquad (22c)$$

$$\dfrac{\partial}{\partial t}(\bar\rho\sqrt{G}\theta) + \nabla\cdot(\Psi\theta)$$
$$= \dfrac{\partial}{\partial x}(\sqrt{G}H_1) + \dfrac{\partial}{\partial\bar z}(\sqrt{G}\,G^{12}H_1 + H_2), \qquad (22d)$$

where the definition

$$\Psi = \bar{\rho}\sqrt{G}u\mathbf{i} + \bar{\rho}\sqrt{G}\omega\mathbf{k} \qquad (23)$$

has been employed. Transformed versions of the elliptic equation for p' [Eq. (15)] and of the defining equation for ω [Eq. (21)] can be constructed similarly. The approach which we have taken in constructing the transformed equations (22) is to effect the transformation upon the independent variables only. It is this restriction upon the transformation which makes it possible to preserve the conservative form for the nonlinear advection terms [e.g., the term $\nabla \cdot (\Psi u)$ in Eq. (22a)]. Lapidus (1967) discusses this point in some generality. This is contrary to the approach in Gal-Chen and Somerville (1975a,b). When the dependent variables are referred to the new coordinate system the transformation of the nonlinear advection terms generates Christoffel symbols of the second kind and since these have no low-order, conservative, finite-difference analogs the energy and momentum budgets of the numerical model are not closed to machine accuracy. In a numerical simulation of wave propagation phenomena it seems judicious to avoid artificial source-sink terms in the algorithm which may conceivably affect the wave energy and momentum.

4. Numerical formulation of the model equations

A detailed description of the finite-difference representations of Eq. (22) is given in Clark (1977), although the analytic forms do not appear there. Only an abbreviated description of the numerical methods will be given here.

The model employs the spatially staggered grid described by Harlow and Welch (1965) for representation of the hydrodynamic fields. Vector components are specified as normal to the grid-box surfaces and all scalars are located at the grid-box center. Quadratically conservative spatial differencing is employed in the numerical formulation of the advective terms in the momentum and internal energy equations where a second-order conservative scheme of Arakawa (1966) is used. These forms conserve momentum to round off error under all conditions and conserve kinetic energy under appropriate conditions.

The pressure and diffusion terms are represented as second-order finite differences. Centered time- and forward time-differencing are applied, respectively, in the representation of advection and mixing. For the specific simulations described in later sections, the spatial sampling intervals are $\Delta x = 600$ m and $\Delta z = 200$ m; a time step $\Delta t = 20$ s is employed, consistent with the Courant-Friedrichs-Lewy criterion for linear stability. The second-order time-differencing scheme for the advective terms requires a start-up procedure. We employ two forward time steps, each of length $\Delta t/2$; the first step is unstable-forward and the second Euler-
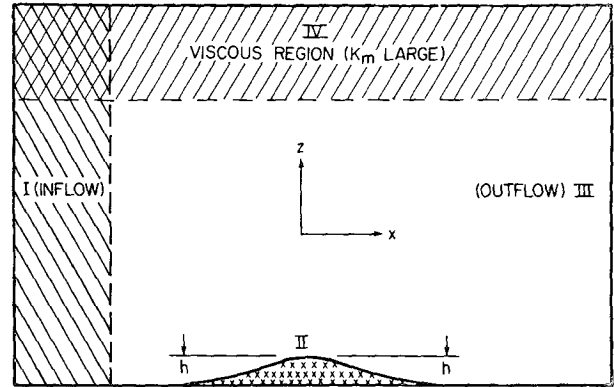

FIG. 1. Domain for the time-dependent nonlinear simulations. The hatched region denotes the volume in which dissipation is artificially enhanced to prevent reflection. Roman numerals I–IV correspond to the four domain boundaries referred to in the text.

backward, the net effect being an extremely slight amplification. To prevent time splitting the integrations are restarted every 20 Δt. The computational domain is 120 $\Delta x \cdot 40$ Δz in size and since the boundary conditions are all treated explicitly, the array size for each hydrodynamic field is $(Nx,Nz) = (122, 42)$.

The finite-difference analog to the transformed version of the pressure equation (15) is solved by applying Ogura's (1969) dimension reduction method (DRM) to transform the elliptic pressure equation to a set of decoupled horizontal Helmholtz equations. The details of this procedure are described in Clark (1977). Truncation errors in the pressure forcing terms in regions of sloping topography result in the introduction of a numerical source-sink due to a slight imbalance between the terms which convert horizontal kinetic energy to vertical kinetic energy. This numerical effect was found to be of the same order or smaller than the nonlinear advection kinetic energy source terms. Typically, less than 1% of the kinetic energy production is associated with it.

5. Boundary conditions for the numerical integrations

A schematic illustration of the domain is shown in Fig. 1 with the boundaries numbered I–IV. We discuss the horizontal boundaries II and IV $(\bar{z}=0,H)$ first and employ Schuman operators (Schuman, 1962) to represent the conditions compactly. We have

$$\omega = 0, \quad \bar{z} = 0, H, \qquad (24a)$$

$$L \approx 0, \quad \bar{z} = 0, H, \qquad (24b)$$

$$\overline{\bar{\rho}^z \omega \bar{w}^z} = 0, \quad \bar{z} = 0, H. \qquad (24c)$$

An approximation to free-slip boundary conditions was employed on $\bar{z}=0,H$. In (24b), L is the vorticity, and

a term involving the vertical derivative of $\omega G^{\frac{1}{2}}$ was ignored so as to avoid the necessity of making the application of the free-slip boundary condition implicit. This was found to be a good approximation and the solutions presented in this paper were in fact completely insensitive to the detail of the boundary condition (24b). When $K_m = 0$ near the lower boundary, as it is in all of the simulations we shall discuss, condition (24b) is in fact redundant. Eq. (24c) is the constraint required to ensure that the vertical integral of the vertical momentum advection be identically zero, i.e., that the domain not leak momentum through the upper and lower boundaries. The conditions on τ_{ij} and H_i on $\bar z = 0, H$ are

$$\overline{\tau_{11}}^z = \overline{\tau_{22}}^z = \tau_{12} = 0, \quad \bar z = 0, H, \quad (25a)$$

$$\overline{H_1}^z = H_2 = 0, \quad \bar z = 0, H. \quad (25b)$$

The second of the thermal boundary conditions (25b) is rigorously nonconducting on $\bar z = 0, H$. We have altered it slightly on $\bar z = H$ to the form

$$H_2 = \frac{\overline{(\bar\rho K_m)}^z}{G}\delta_z\langle\theta'\rangle, \quad \bar z = H, \quad (25c)$$

where $\langle\theta'\rangle$ is the horizontal average of θ'. This is done to suppress cooling in the upper regions of the model where K_m (and thus $K_H = K_m$) is made artificially large in order to prevent the downward reflection of upward propagating internal waves generated by the mountain.

As mentioned above, K_m is artificially enhanced in the upper levels of the model to inhibit reflection. This region is shown hatched in Fig. 1. The thickness of this region has been taken to be on the order of one vertical wavelength $(H - D \approx \lambda_z)$ and the diffusivity within it to increase sinusoidally from zero at $\bar z = D$ to a maximum at $\bar z = H$. Thus, explicitly

$$K_m = K_m^0\left\{1 - \cos\left[\frac{\pi}{2}\frac{(\bar z - D)}{(H - D)}\right]\right\}, \quad D < \bar z < H. \quad (26)$$

The constant K_m^0 was chosen such that the amplitude of a plane internal wave with vertical wavelength λ_z would be reduced by $\sim 95\%$ in the process of traversing the viscous layer. This method of preventing reflection was found to be extremely effective although it wasted a large fraction (~ 0.25) of the full domain height. In particular it seems to be a better method of suppressing reflection than the "Rayleigh friction" formulation (a linear drag law) employed in Clark (1977). The effect of the viscous layer as a wave absorber is seen clearly in the vertical profiles of Reynolds stress to be described in Section 7.

The conditions at the lateral boundaries of inflow and outflow (I and III, respectively, in Fig. 1) are chosen in accord with the linear lee wave problem described in the next section. At the inflow boundary, free slip conditions are employed on the dynamic variables such that

$$\left.\begin{array}{ll}\delta_x\theta' = \delta_x w = 0, & x = x_I \\ u = u_0(z), & x = x_I \\ \overline{[u - u_0(z)]}^x = \overline{u'}^x = 0, & x = x_I\end{array}\right\}, \quad (27)$$

where $x = x_I$ is the location of the lateral inflow boundary. In addition a Newmann-type boundary condition for the pressure perturbation p' is derived to satisfy the constraint

$$\overline{\delta_t(\bar p^x u)}^t = 0, \quad x = x_I. \quad (28)$$

These conditions at the inflow boundary assume, in effect, that the upstream disturbance vanishes and $x = x_I$ is taken sufficiently far upstream that this assumption is justifiable. That this assumption is rigorously valid in the linear limit is well known. The remaining variables have zero horizontal gradient at $x = x_I$ for all $\bar z$. It was found that keeping $\theta' = \theta'(z)$, the profile at $t = 0$, was numerically unstable when the static stability was strong.

A viscous absorbing region of width 20 Δx was also employed at the inflow boundary to absorb upstream propagating transients as well as any weak upstream steady-state disturbance produced by blocking at the mountain. It is assumed that this viscous region will effectively make the inflow boundary appear, in a numerical sense, to be infinitely distant from the mountain to the nonlinear, upstream propagating features of the flow. The form employed for K_m at the inflow boundary was similar to (26) and the same value of K_m^0 was assumed.

At the outflow boundary (III in Fig. 1) we employ an extrapolation scheme which approximates to the Sommerfeld condition and is similar to one recently described by Orlanski (1976). The necessity of this derives from the fact that during initialization of the model, even if the mean flow is accelerated smoothly from rest to its steady upstream amplitude, there are significant transients generated. When these transients strike the downstream boundary they will, unless special care is taken, be reflected back into the domain interior and severely contaminate the integration.

The inflow-outflow boundary conditions just described were critical to the success of the numerical simulations. The dynamical effects which concern us demand for their proper representation a model with aperiodic lateral boundary conditions. When wave-mean flow interaction occurs the net effect is an irreversible modification of the inflow momentum profile, an effect which the use of periodic boundary conditions excludes. In the next section we obtain a simple linear

steady-state solution against which the performance of the numerical model will be calibrated.

6. A linear steady-state solution: Uniform wind and stability

Here we present briefly an analytic solution to the linear, inviscid, steady-state form of the governing equations (1)–(3). We will not describe its derivation in detail since the methods of linear theory are well known. It will be employed subsequently to verify in detail the validity of the numerical model in the steady state when the wave amplitude is small and, furthermore, will be restricted to the solutions for uniform flow over a bell-shaped mountain when the background atmosphere has constant Brunt-Väisälä frequency. The two-dimensional topography is represented as

$$z_s(x) = \frac{a^2 h}{x^2 + a^2} \tag{29}$$

which has the simple spectral representation

$$Z_s(k) = \pi a h e^{-ak}, \tag{30}$$

where k is the horizontal wavenumber, and a is the half-width of the obstacle at half its maximum height h. If $w(x,z)$ is the vertical perturbation velocity we may represent it in terms of the steady-state free-stream deflection $\xi(x,z)$ such that

$$w = U_0 \frac{\partial \xi}{\partial x}. \tag{31}$$

The linear steady-state solution satisfying the radiation condition as $z \rightarrow \infty$ and the *linear* boundary condition

$$w = w_0 = U_0 \frac{\partial z_s}{\partial x}, \quad z = 0, \tag{32}$$

has the form (Lyra, 1943)

$$\xi(x,z) = \pi^{-1} \exp(z/2H)$$

$$\times \int_C \exp i[kx + (k_G^2 - k^2)^{\frac{1}{2}} z'] Z_s(k) dk, \tag{33}$$

with

$$k_G^2 = \frac{(N^2/U_0^2) - (\omega_a^2/c^2)}{[1 - (U_0^2/c^2)]}, \tag{34a}$$

$$z' = [1 - (U_0^2/c^2)]^{\frac{1}{2}} z, \tag{34b}$$

where C is the contour $0 < k < \infty$ along the real axis in the complex k-plane and where ω_a is the acoustic cutoff frequency $(\omega_a = g/2c)$. In the limit of low Mach number $(M = U_0/c \ll 1)$ the solution (33) is exactly compatible with the first-order perturbation equations deduced from (1)–(3). In (33) H is the *isothermal* scale height.
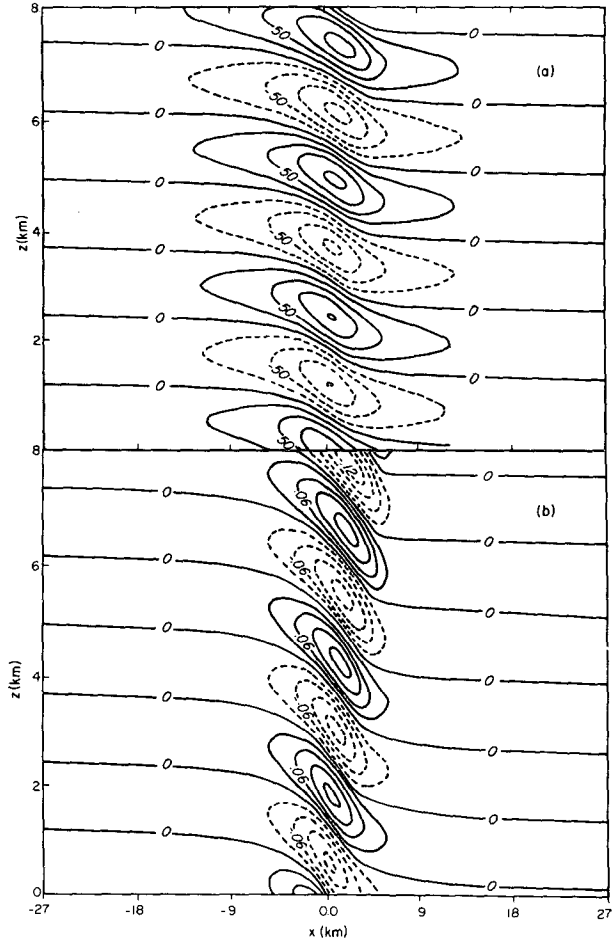

Fig. 2a. Contours of constant (steady state) free stream deflection $\xi(x,z)$ based upon linear inviscid theory. (Dashed line = negative ξ; solid line = positive ξ). Parameters $2\pi/N = 10.2$ min, $U_0 = 4$ m s^{-1}, $a = 3$ km, $h = 100$ m.

Fig. 2b. Contours of constant (steady state) vertical velocity $w(x,z)$ deduced from $\xi(x,z)$ in (a), where $w = U_0 \partial \xi / \partial x$. (Dashed line = negative w; solid line = positive w).

With $M \ll 1$

$$\left. \begin{array}{l} k_G^2 \approx N^2/U_0^2 \\ z' \approx z \end{array} \right\}. \tag{35}$$

With $Z_s(k)$ as in (30) it is straightforward to obtain $\mathrm{Re}(\xi)$ corresponding to the physical disturbance in terms of simple real integrals. These representations, valid, respectively, in the downstream $(x > 0)$ and the upstream $(x < 0)$ regions, are

$(x > 0)$:

$$\mathrm{Re}(\xi) = a h e^{z/2H} \left[k_G \int_0^{\pi/2} d\beta \cdot \cos\beta \cdot \exp(-ak_G \sin\beta) \right.$$

$$\times \cos[r \cos(\beta - \omega)] + k_G \int_0^\infty d\Psi \cdot \exp(-ak_G \cosh\Psi)$$

$$\left. - \cos\omega \cosh\Psi \cdot \sinh\Psi \cdot \cos(r \sin\omega \cosh\Psi) \right] \tag{36a}$$

$(x<0)$:

$$\mathrm{Re}(\xi) = ahe^{z/2H}(-1/x)\int_0^\infty d\lambda e^{-\lambda}\,'$$

$$\times\sin\left[\frac{-a\lambda}{x}+\left(k_G{}^2+\frac{\lambda^2}{x^2}\right)^{\frac12}z\right].$$

where

$$\left.\begin{array}{c}k_Gx=r\sin\omega\\ k_Gz=r\cos\omega\\ k=k_G\sin\beta\end{array}\right\} \qquad (36b)$$

provide the definitions of ω and β in (36a).

The field $\mathrm{Re}(\xi)$ deduced by Gaussian quadrature on the integrals (36) and with the parameters $a=3$ km, $U_0=4$ m s^{-1}, $2\pi/N=10.2$ min is shown in Fig. 2a. The corresponding w field is determined from (31) using centered finite differences and is shown in Fig. 2b. It is clear from (36) that the amplitude of the vertical velocity field scales linearly with the mountain height h. The single nondimensional parameter in this simple linear mountain wave problem is thus the

Froude number Fr, which we shall define as

$$\mathrm{Fr}=\frac{(2\pi/N)}{(2a/U_0)}, \qquad (37)$$

the ratio of the Brunt-Väisälä period to the launching period of the internal waves. So long as $\mathrm{Fr}<O(1)$ the fluid response to the forcing from below consists of a freely propagating internal wave field as in Fig. 2. For $\mathrm{Fr}\gg 1$ the response is entirely evanescent and the disturbance is trapped in the region of forcing. With the parameters U, a and N as above $\mathrm{Fr}\approx 0.408$.

Associated with the wave field (36) there is a drag on the air near the surface and a related force on the earth which we may calculate from the linear steady state form of the horizontal momentum balance equation [(1) with $K_m\equiv 0$]. This is just

$$D_w(0) = -\rho_0\int_{-\infty}^{+\infty} u'w'dx = -\int_{-\infty}^{+\infty} z_s(x)\frac{\partial p}{\partial x}dx \qquad (38)$$

which is the negative of the Reynolds stress integrated over the surface $z=0$. The Eliassen-Palm theorem (Eliassen and Palm, 1960) assures us furthermore under
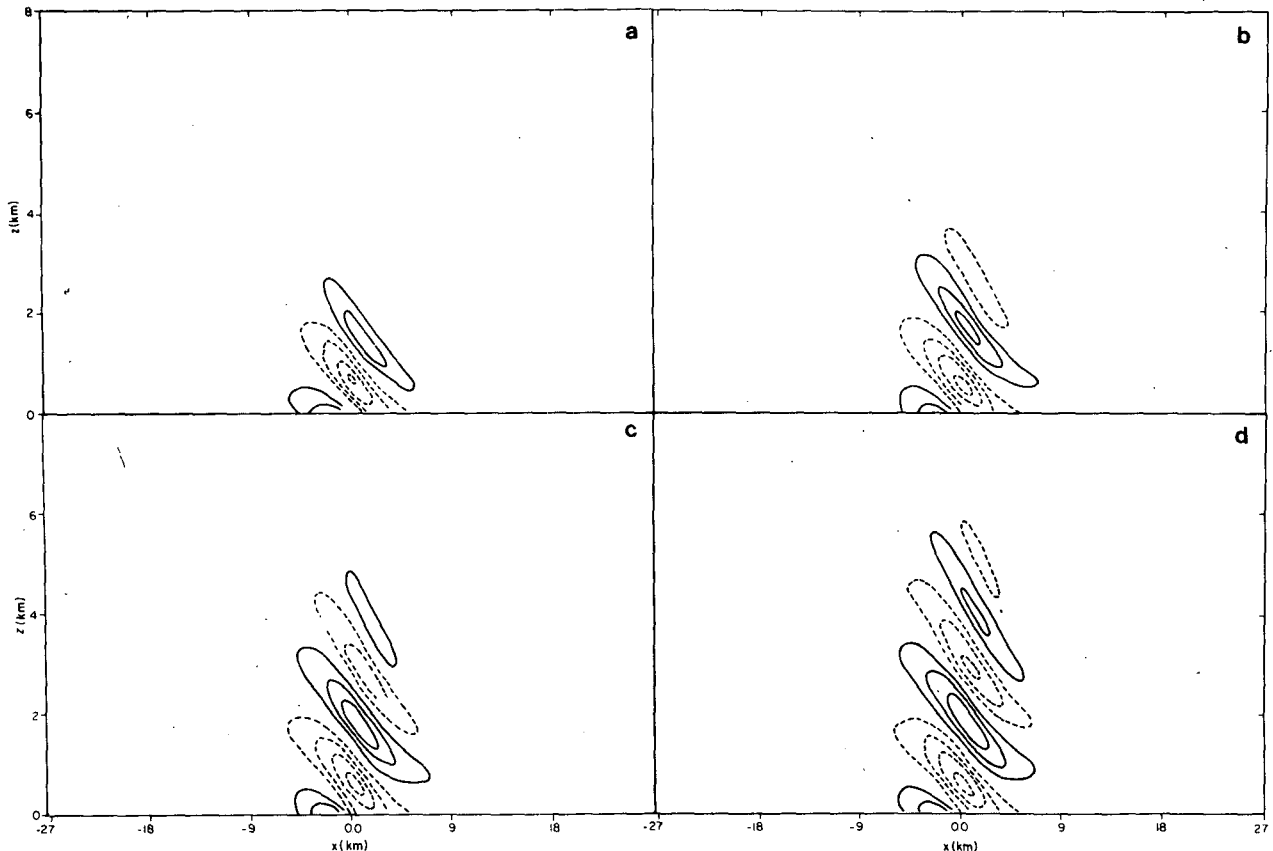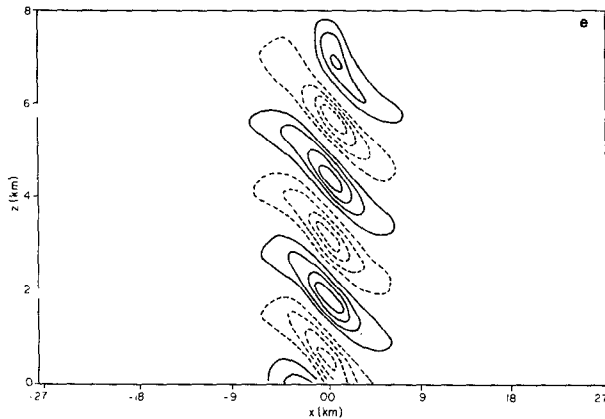

FIG. 3. Temporal evolution of the vertical velocity field from the nonlinear model with $2\pi/N=10.2$ min, $U_0=4$ m s^{-1}, $a=3$ km, $h=100$ m. The individual plates correspond to the times (a)$=240\ \Delta t$, (b)$=280\ \Delta t$, (c)$=320\ \Delta t$, (d)$=360\ \Delta t$, (e)$=1020\ \Delta t$ (steady state). Plate (e) should be compared with Fig. 2b. The time step $\Delta t = 20$ s.

the present circumstances (no wind reversal aloft) that

$$\frac{\partial}{\partial z}\left(\rho_0 \int_{-\infty}^{+\infty} u'w' dx\right) \equiv 0; \qquad (39)$$

thus the mean flow above the surface will never feel the wave drag so long as the wave amplitude is small. From (38), (36) and (31) we may obtain a closed form expression for $D_w(0)$ in (38) as

$$D_w(0) = \rho_0 \pi a^2 h^2 U^2 \int_0^{k_G} dk e^{-2ak} k(k_G{}^2 - k^2)^{\frac{1}{2}}. \qquad (40)$$

It is clear from (40) that only the freely propagating part of the wave spectrum contributes to the surface drag.

In the finite-amplitude regime we may expect the linear solution (36) to become increasingly invalid as the aspect ratio of the topography $A = h/a$ increases keeping the Froude number fixed. We expect two effects to be important: (i) on the assumption of no upstream influence the vertical profile of Reynolds stress should become increasingly divergent near the ground to account for the effect of the nonlinear lower boundary condition; and (ii) the linear solution should become unstable convectively for A sufficiently large that the vertical gradients of perturbation potential temperature are sufficiently large and negative (in alternate vertical phases of the wave) that the background stability is erased. In the following section we shall compare the predictions (36), (39) and (40) of linear steady-state theory to the nonlinear time-dependent simulations using the model described in Sections 2–5 and will in particular focus upon the demonstration of hypotheses (i) and (ii) above.

7. Finite-amplitude time-dependent solutions

a. The small aspect ratio limit

We describe the nonlinear transient evolution of the wave field at Froude number Fr=0.408 as in the last

section. The magnitude of the Brunt-Väisälä period $2\pi/N$ corresponds to a vertical gradient of potential temperature $d\theta_0/dz \approx 3°C$ km^{-1} in accord with the observed mean stability of the troposphere. In order to reduce the amplitude of transients generated during the initialization of the numerical integrations the mean flow is accelerated linearly from rest to its steady value $U_0 = 4$ m s^{-1} over a time t_s which is such that $t_s > O(2\pi/N)$. This procedure does not eliminate such transients but it does severely attenuate their amplitudes.

The number of grid points in the domain is kept fixed at $Nx \cdot Nz = 122 \times 42$ and the grid spacing employed is $\Delta x = 600$ m, $\Delta z = 200$ m. The domain is thus 8 km high and 72 km long. From Fig. 2 we see that this resolution is sufficient to give approximately 12 grid points per wavelength in the vertical. Increased resolution does not affect the numerical results at the 3% level. The mountain profile is again given by (29) but the topographic maximum is offset in the domain by a distance equivalent to 30 horizontal grid intervals in the downstream direction. This offset was included to maximize the distance of the obstacle from the inflow boundary and thus to reduce the tendency at this boundary toward the formation of a spurious upstream disturbance. The first 20 intervals are for viscous absorption as discussed previously.

In Fig. 3 we show a series of time slices through the evolving two-dimensional vertical velocity field forced by a mountain with $h = 100$ m so that $A = 1/30$. In the long time limit as the field approaches its steady-state expression this solution may be compared visually to the linear result in Fig. 2. The vertical wavelength $\lambda_z = 2\pi/k_z$ of the disturbance agrees to within a few percent with the linear result. From the Boussinesq form of the plane wave dispersion relation for the
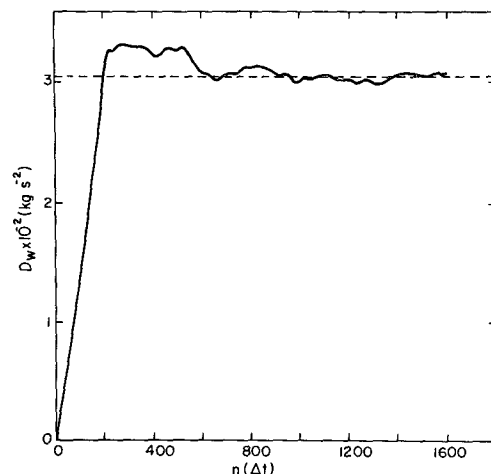

Fig. 4. Temporal evolution of the surface drag (force on the earth per unit area per unit length). The dashed line is the result from linear steady state theory. Parameters are the same as in Fig. 3.
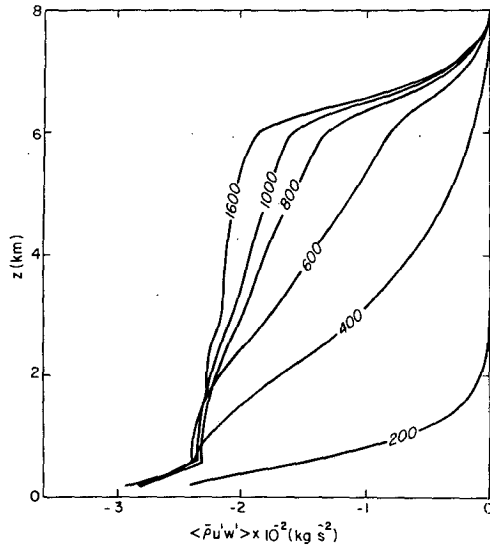
FIG. 5. Temporal evolution of the Reynolds stress $\bar{\rho}u'w'$ as a function of height z. The time is in units of $\Delta t = 20$ s. Note that in the long time limit the Reynolds stress in the interior becomes nondivergent in accordance with the prediction of the Eliassen-Palm theorem.

steady disturbance,

$$k_z^2 = \frac{N^2}{U^2} - k^2. \tag{41}$$

Since $N^2/U^2 \gg k^2$, the wave is almost hydrostatic with

$$k_z \approx N/U \tag{42}$$

and thus $\lambda_z \approx 2.45$ km as in Figs. 2 and 3.

A more stringent test of the validity of linear theory in the small aspect ratio limit concerns the second-order results (38), (39) and (40). In Fig. 4 we compare the temporal evolution of the surface drag to that predicted by the linear theory (40). The surface drag overshoots the linear prediction following the 200 Δt start-up period after which it settles smoothly upon the analytic result and oscillates with very small amplitude about it. The overshoot is produced by transients generated in initialization. Without the smooth starting procedure the overshoot and the ensuing oscillations have larger amplitude. The smooth start-up procedure was in fact designed to eliminate these effects.

In Fig. 5 we show the temporal evolution of the vertical profile of Reynolds stress [the negative of the first integral in (38) as a function of height]. Far from the boundary and in the long time limit the stress profile becomes nondivergent as predicted by the Eliassen-Palm theorem (39). There are, however, two regions of divergence in the profile adjacent to the upper and lower domain boundaries. The first of these, near the upper boundary, is a necessary artifact of the presence of the viscous absorption region described by Eq. (26). The slight divergence of the stress profile in the low levels

is due to the nonlinearity of the lower boundary condition (i.e., $\omega = 0$ on $\bar{z} = 0$ rather than $w = U_0 \partial z_s / \partial x$ on $z = 0$). The sense of this divergence is such that counterflow momentum is absorbed. If $\langle \bar{\rho}u'w' \rangle$ is extrapolated down to $z = 0$ through the region of divergence then $-\langle \bar{\rho}u'w' \rangle = D_w$. This is convincing evidence that the surface divergence is "real."

In the next section a further effect of this nonlinearity at the lower boundary will be described when we plot the temporal evolution of the perturbation velocity tangential to the surface as a function of horizontal position through the nondimensional "down-slope wind amplification factor" which we define as

$$\frac{U_T - U_0}{U_0}. \tag{43}$$

As we shall see from this function the maximum tangential wind speed is obtained just to the lee of the mountain crest. Furthermore, we shall show that in the long time limit the factor (43) is larger than zero at the downstream boundary so the outflow at the surface is accelerated, i.e., counterflow momentum is extracted irreversibly from the low levels.

Comparing Figs. 4 and 5 we note that accompanying these nonlinear effects at the lower boundary there is now a mismatch between the magnitude of the surface stress and the uniform Reynolds stress in the interior in the long time limit. The effect is such that the wave momentum flux in the upper levels is smaller than would be predicted on the basis of linear theory which demands equality between these two quantities. The amount of the reduction is $\sim 20\%$ for $A = 1/30$. This effect is entirely due to the nonlinearity of the lower boundary condition which even for $A = 1/30$ is sufficient
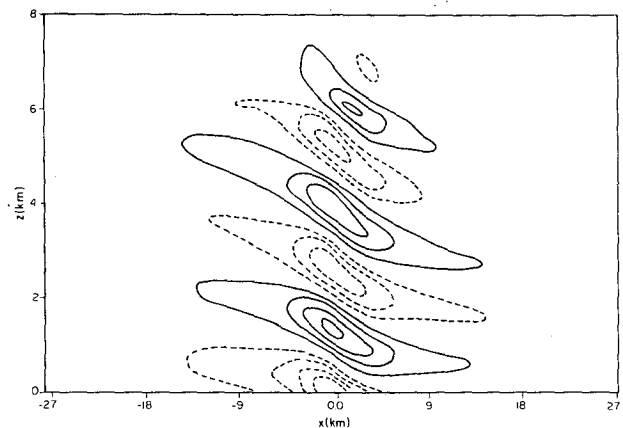

FIG. 6. Steady-state potential temperature perturbation $\theta''(x,z)$ [where $\theta = \bar{\theta} + \theta'$, $\theta''(x,z) = \theta'(x,z) - \langle \theta' \rangle$, and $\langle \theta' \rangle$ denotes the z-dependent horizontal average of θ']. The time is 1020 Δt corresponding to the vertical velocity field in Fig. 3e. Compare with Fig. 2a for the linear $\xi(x,z)$ field and note the validity of the proportionality $\theta''(x,z) = -(d\langle \theta \rangle/dz)\xi(x,z)$ predicted by linear theory.

to affect the second-order characteristics of the wave system. With the exception of this physically explicable effect we feel justified in claiming that for A sufficiently small the numerical model agrees extremely well with the predictions of linear theory in the steady-state, long time limit.

b. Aspect ratio dependence of bow evolution and stability

Fig. 6 illustrates the steady form of the perturbation potential temperature field in the case $A = 1/30$ described in Section 7a. The phase characteristics of this field clearly mimic those shown previously (Fig. 2a) for the free stream deflection. The first half-vertical wavelength corresponds to the increase in θ which is forced by the descent of fluid in the lee of the mountain. This is a purely adiabatic effect since $K_H = 0$ in these simulations (away from the upper boundary). Similarly the second half-vertical wavelength has an associated θ perturbation which is negative corresponding to the cooling upon adiabatic ascent in the second half-vertical wavelength of the w field. Clearly, since ξ and thus w scales as h there will exist a critical aspect ratio A_c above which the vertical gradient of θ will become locally superadiabatic and the wave will become convectively unstable. In terms of the temporal evolution of the wave system this instability will always exist regardless of A on account of the height growth factor $\exp(z/2H)$ in (36). Of dominant concern in the geophysical problem is the value of $A = A_c$ at which this instability is triggered in the first vertical wavelength.

We may employ the linear solution (36) to construct an a posteriori stability criterion for the determination of A_c and thus h_c with a held fixed. The linearized form of the steady-state version of (3) is just (where subscript 0 refers to the basic state of linear theory)

$$U_0 \frac{\partial \theta'}{\partial x} + w \frac{d\theta_0}{dz} = 0. \tag{44}$$

Since, in the steady state, we may define w in terms of the free-stream deflection ξ by (31), Eq. (44) is thus equivalent to

$$\frac{\partial \theta'}{\partial x} + \frac{\partial \xi}{\partial x} \frac{d\theta_0}{dz} = 0. \tag{45}$$

Under the assumption of no upstream influence (45) integrates directly to give

$$\theta'(x,z) = \frac{-d\theta_0}{dz} \xi(x,z). \tag{46}$$

The a posteriori stability condition is thus

$$\left(\frac{-\partial \theta'}{\partial z}\right)_{\max} \approx \frac{d\theta_0}{dz}\left(\frac{\partial \xi}{\partial z}\right)_{\max} > \frac{d\theta_0}{dz}, \tag{47}$$
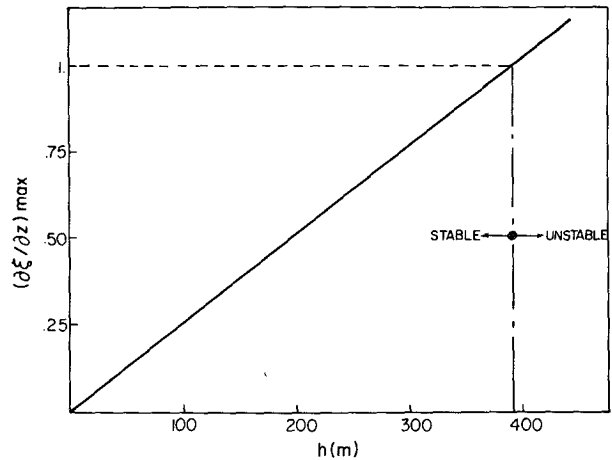

FIG. 7. Stability diagram based upon the a posteriori condition deduced from linear theory. For $(\partial \xi/\partial z)_{\max} > 1$ the wave is convectively unstable.

if $d\theta_0/dz$ is approximately constant as in the present model. This condition, which expresses the physical requirement that the fluctuation potential temperature gradient be just sufficient to offset the background stability, can be written more simply as

$$\left(\frac{\partial \xi}{\partial z}\right)_{\max} \geqslant 1. \tag{48}$$

In Fig. 7 we plot $(\partial \xi/\partial z)_{\max}$ as a function of h and note that condition (48) is satisfied for the first vertical wavelength of the wave system for $h \gtrsim 400$ m, i.e., for an aspect ratio $A_c = 2/15$. We proceed to test this prediction with the nonlinear model and to investigate the flow characteristics in the unstable regime.

In Fig. 8 we compare the wave drag on the surface with the linear prediction for $h = 200$, 300 and 400 m. In the first two cases, although the overshoot of the wave drag following start-up is still apparent, at the end of the integration period its magnitude is decreasing slowly toward an asymptote which is close to the linear prediction although somewhat in excess of it. For $h = 400$ m the wave drag continues to increase following the initialization phase and in the later stages begins to oscillate with a magnituade which is approximately 100% in excess of the linear prediction. We associate this increased surface drag with an increased pressure drop across the topography which is induced by the onset of convective instability in the wave.

Fig. 9 shows the temporal evolution of the vertical Reynolds stress profile for $h = 200$, 300, 400 m. The divergence of the stress profile in low levels is still apparent, as is the decrease in launching efficiency associated with the nonlinear lower boundary condition. For $h < 400$ m, however, in the domain interior the Reynolds stress profile remains nondivergent in the long time limit and thus so long as the wave field is
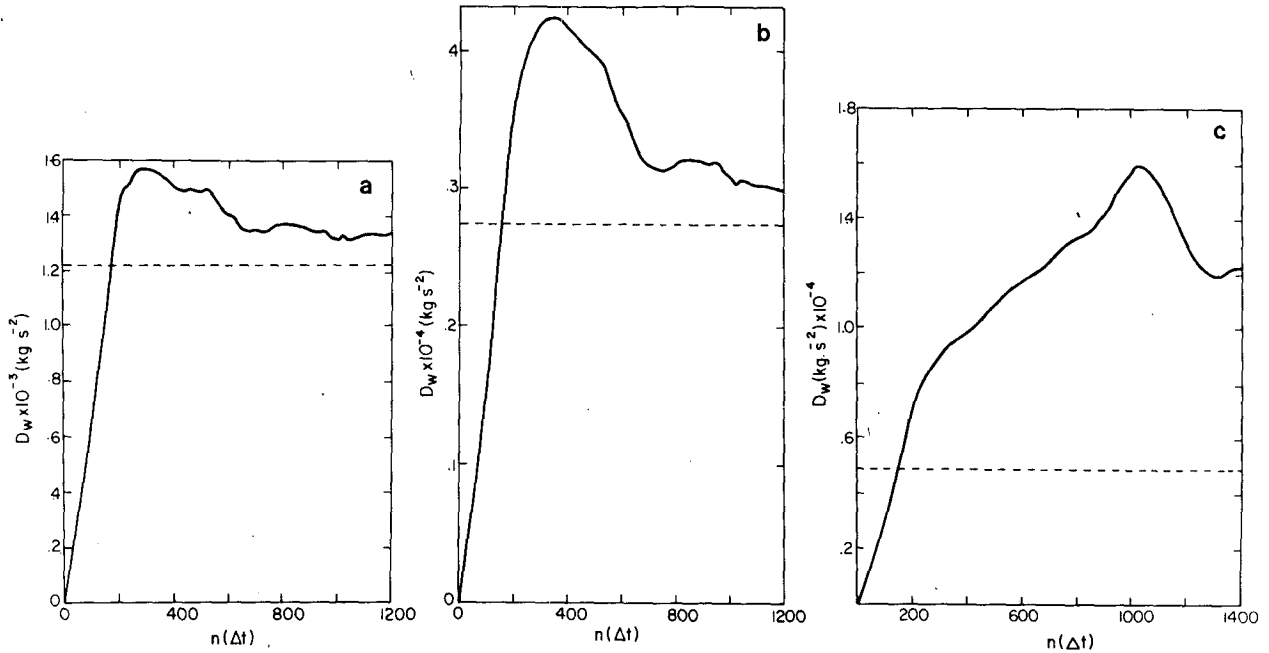
FIG. 8. Temporal development of the surface wave drag for (a) $h=200$ m, (b) $h=300$ m, (c) $h=400$ m. Note the large increase in drag in the unstable regime (excess of the linear prediction) for $h=400$ m. Dashed line is the linear result.

convectively stable the Eliassen-Palm theorem continues to hold. For $h=400$ m a marked divergence of the stress profile accompanies the increased surface drag, implying a strong wave-mean flow interaction away from the lower boundary. In Table 1 we compare the asymptotic Reynolds stress in the interior to the surface drag and note that the mismatch is $\sim 20\%$ for $h<400$ m.

The temporal evolution of the downslope wind amplification is shown for the three values of h in Fig. 10. Again the acceleration above the inflow speed at the outflow boundary is noted. For $h=400$ m there is a continuous increase in the maximum tangential wind speed at the surface following initialization, which is in accord with the increased pressure drop across the topography induced by the onset of convective instability and the increased surface drag.

In Fig. 11 we illustrate the temporal evolution of the vertical velocity field for $h=400$ m and note the marked splitting of the phase structure which is produced by the instability. The intensity of the wave-induced convection was inhibited in this simulation through the use of the first-order closure scheme (12b)
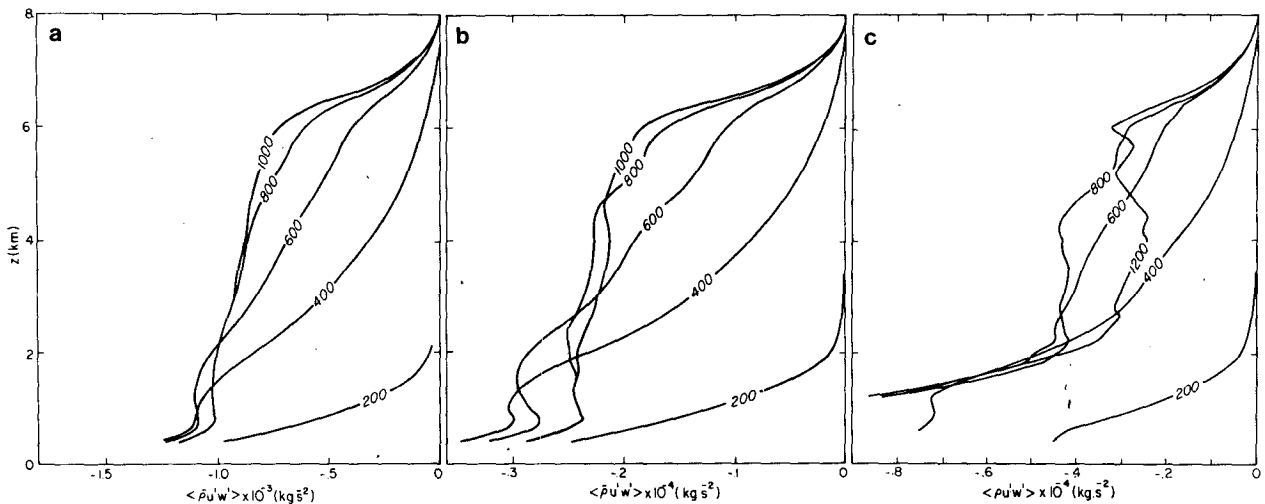

FIG. 9. Reynolds stress profile as a function of time for (a) $h=200$ m, (b) $h=300$ m, (c) $h=400$ m. Note the strong divergence in the interior in the unstable regime for $h=400$ m.

for the momentum diffusivity. This control on the strength of the convective circulation embedded in the wave acts such as to minimize the effects of the instability previously enumerated. The temporal evolution of K_m is illustrated in Fig. 12 where we plot $K_m^{max}(t)$. The maximum value of K_m occurs at a height $\lambda_z/2$ above the surface which is just the location cited previously as that at which the convective instability should first appear; K_m remains zero everywhere surrounding the region of instability. In Fig. 12 we further note that even the initial transient is sufficiently strong to "switch on" a small amount of mixing. However this soon decays to zero and does not reappear until the steady signal has been established in the region $\lambda_z/2 < z < \lambda_z$.

8. Summary and conclusions

We have presented a very small fraction of the numerical data which has been collected during this initial study of the evolution and stability of finite-amplitude mountain waves, and have concentrated the discussion on the nonlinear effects which occur in uniform means flows with homogeneous stratification. In the limit that the aspect ratio of the obstacle is small the nonlinear numerical model is in almost exact accord with the predictions of linear theory, even with respect to the magnitude of certain second-order characteristics of the flow (e.g., the surface wave drag). In this limit the vertical profile of Reynolds stress sufficiently far from the lower boundary is nondivergent as predicted by the Eliassen-Palm theorem. In the lower levels the stress profile is slightly divergent and there is therefore a mismatch between the surface drag and the uniform stress level in the interior. The discrepancy is such that the wave amplitude in the interior is lower by approxi-

TABLE 1. Comparison of wave drag on the surface to Reynold stress in the interior.

h (m)	$D_w(t \to \infty)$ (kg s^{-2})	$\langle \bar{\rho} u'w' \rangle (t \to \infty)$ (kg s^{-2})	Percent mismatch
100	3.05×10^2	-2.40×10^2	21.3
200	1.30×10^3	-1.05×10^3	19.2
300	3.00×10^3	-2.40×10^3	20.0
400	$\sim 1.30 \times 10^4$	unstable (no asymptote)	—

mately 10% than the linear predictions in the small aspect ratio $(A = 1/30)$ case. This discrepancy is not a strong function of aspect ratio. For $h < h_c$ (the critical height for the onset of convective instability) the stress profile remains nondivergent in the interior in spite of the fact that the wave amplitude is large.

For $h > h_c (h_c \approx 400$ m with $a = 3$ km, $2\pi/N = 10.2$ min, $U_0 = 4$ m s^{-1}) the wave becomes convectively unstable and the flow highly unsteady. The *a posteriori* stability condition

$$\left(\frac{\partial \xi}{\partial z}\right)_{max} \geqslant 1$$

deduced from linear theory was found to provide an accurate estimate of h_c and thus (with a fixed) of the critical aspect ratio. This condition for the onset of convection is equivalent to that for which an overhead streamline first becomes vertical and has been employed previously in explanation of the appearance of "rotors" in the wave field (e.g., Long, 1955; Miles and Huppert, 1969; Danielson and Bleck, 1970). In the unstable regime the wave drag on the surface increases, the maximum strength of the downslope flow in the lee
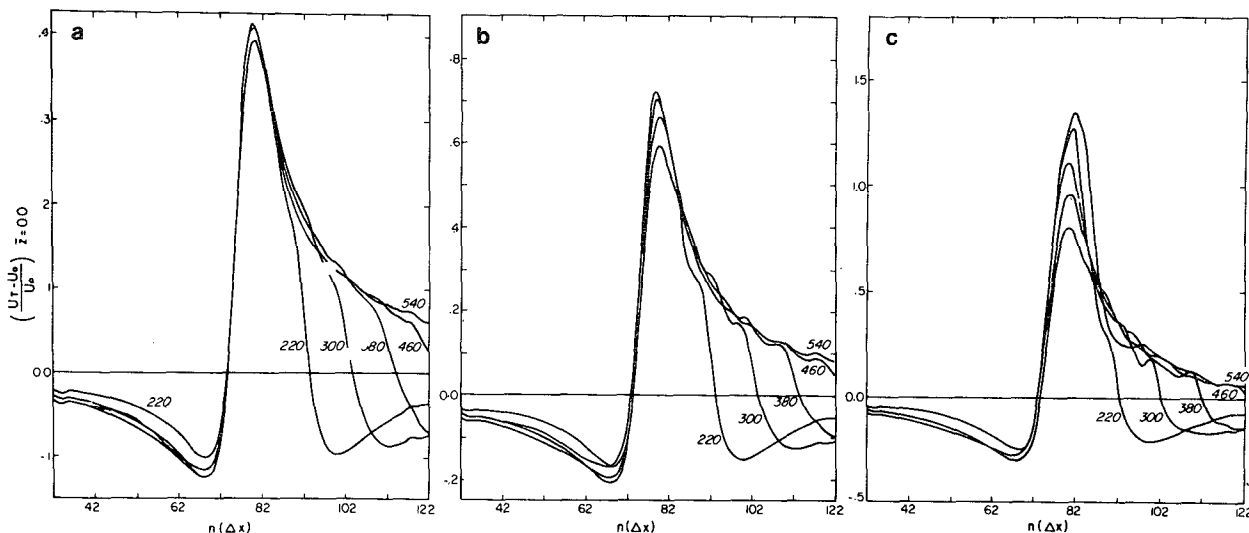

FIG. 10. Time development of the downslope wind amplification factor, with the time in units of $\Delta t = 20$ s for (a) $h = 200$ m, (b) $h = 300$ m, (c) $h = 400$ m. Note the increase in the maximum tangential wind speed at the surface in the unstable regime with $h = 400$ m.
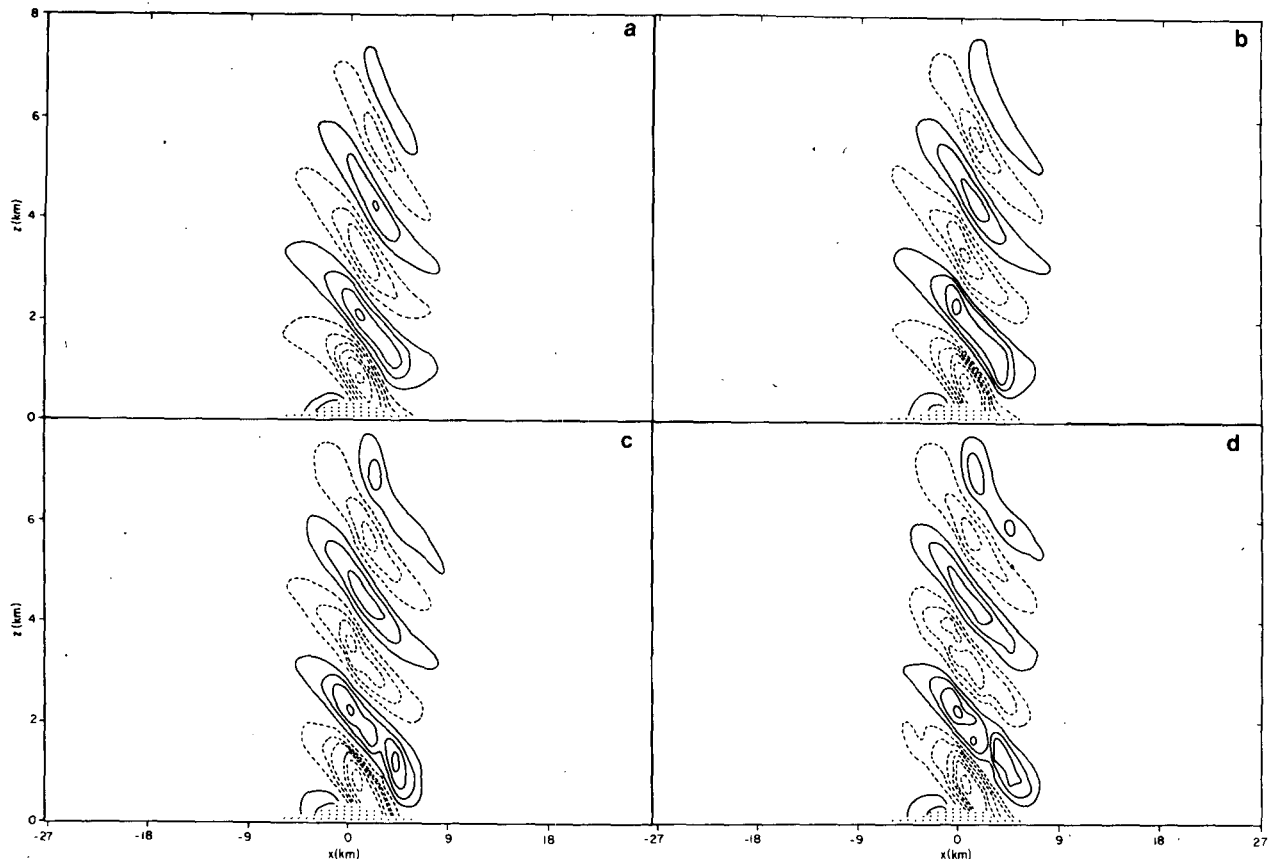
FIG. 11. Temporal evolution of the vertical velocity field with $h=400$ m for (a) $t=420\ \Delta t$, (b) $t=460\ \Delta t$, (c) $t=500\ \Delta t$, (d) $t=540\ \Delta t$. Note the pronounced splitting of the phase structure produced by the onset of convective mixing.

increases, and the Reynolds stress profile becomes strongly divergent implying a strong wave-mean flow interaction.

The implications of these results for the geophysical problem require some further remarks. Although the value of N which we employed is reasonable as a measure of mean tropospheric stability, the parameters $U_0=4$ m s^{-1} and $a=3$ km are both too small. From (42) increasing U_0 increases the vertical wavelength and from (32) it also increases the wave amplitude. To keep Fr small and the response in the internal wave regime with U_0 large demands a commensurate increase of the half-width a from (37). Since the amplitude is proportional to h/a from (32), if condition (48) is to be satisfied with a large then the mountain height h must also be increased.

One of the main characteristics of the strong wave events described by Lilly and Zipser (1972) is that the vertical wavelength of the observed wave field is roughly equal to twice the tropopause height so that the tropopause is a distance $\lambda_z/2$ above the surface. This condition has been invoked by Klemp and Lilly (1975) in explanation of the occurrence of strong downslope windstorms. The tropopause is a boundary at which strong partial wave reflections occur because of

the rapid increase of stability there. When the elevation of this surface is $\lambda_z/2$ there is constructive interference between the direct and reflected waves at the surface and thus a strong surface response. With $2\pi/N=10.2$ min we need $U_0\approx25$ m s^{-1} to give $\lambda_z/2\approx$ tropopause
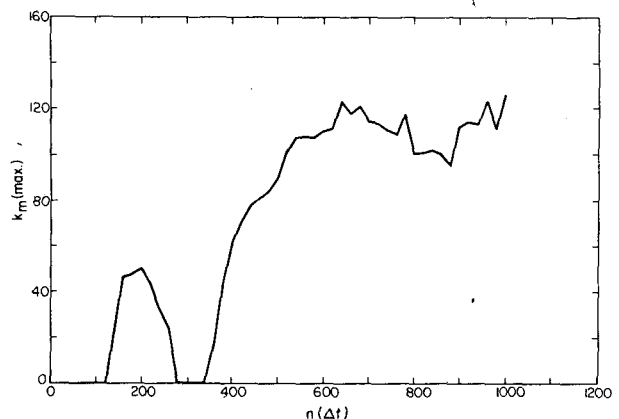

FIG. 12. Development with time (in units of $\Delta t=20$ s) of the maximum value in the domain of the momentum diffusivity K_m. This maximum is obtained a distance $\lambda_z/2$ above the surface and slightly to the lee of the mountain crest. Note that $K_m^{\max}$ is increasing rapidly as the wave breaks (cf. Fig. 11).

height. If we employ this value of U_0 to rescale our results and take $a \approx 12$ km (an estimate of the half-width of the peak generating the internal wave in the Lilly and Zipser observations) then to satisfy the *a posteriori* stability condition we require an obstacle elevation in excess of 1 km. This is satisfied by the topography associated with the observed wave field. The wave may therefore be unstable a distance $\lambda_z/2$ above the surface. In the data described by Lilly and Kennedy (1973) this is the height at which the magnitude of the Reynolds stress decreases to zero. It is also the height at which severe turbulence was encountered by the aircraft employed to make the *in situ* flux measurements. On the basis of the results reported here we would interpret the observations as indicating that the wave amplitude was super-critical with respect to the criterion for convective stability. This might explain both the location of turbulence in the region $\lambda_z/2$ above the surface and the strong divergence of the stress profile there.

We suspect that the preceding interpretation of the Lilly and Zipser (1972) data will require some modification when the effects of vertical shear in the mean flow and vertical variations of stability are taken into account. However, the main fact which our calculations have demonstrated is not liable to be strongly modified by the simulation of more complicated systems. The geophysical circumstances in which a lee wave becomes convectively unstable within the first vertical wavelength should be rather common in the atmosphere. When such circumstances obtain there exists an alternative mechanism to the one advanced by Klemp and Lilly (1975) which is potentially capable of explaining the phenomenon of strong downslope winds.

When the wave induces the superadiabatic condition at a height $\sim \lambda_z/2$ above the surface, this region once established, will act as a strong reflector of incident wave energy. The reflectivity at this height is not due, however, to the negative lapse rate but is rather associated with the nonlinear critical layer which is established simultaneously. Since the velocity field is approximately solenoidal (Boussinesq approximation), this can be seen by direct inspection of the continuity equation

$$\frac{\partial u'}{\partial x} + \frac{\partial w'}{\partial z} = 0,$$

where the total horizontal wind field is

$$u^* = U_0 + u'.$$

Expressing w' in terms of ξ as in (31), the continuity equation, with the assumption of no upstream influence, may then be integrated directly to give

$$u' = -U_0 \frac{\partial \xi}{\partial z}.$$

Therefore the total horizontal wind is

$$u^* = U_0 \left(1 - \frac{\partial \xi}{\partial z}\right),$$

and wherever the flow is locally superadiabatic ($\partial \xi / \partial z > 1$) a critical layer also exists, i.e., there is a wind reversal aloft. At such a local critical level the gradient Richardson number is necessarily such the $\mathrm{Ri} < 0.25$. Davis and Peltier (1976, 1977) have shown that such a critical level has a reflectivity which exceeds unity irrespective of whether the flow is inviscid or dissipative. When $(\partial \xi / \partial z)_{\max} > 1$ the nonlinear mountain wave will amplify between its critical level and the ground via the mechanism of multiple overreflection (Davis and Peltier, 1976). This resonant amplification will force a continuous growth in time of the wave drag on the surface and a concomitant continuous increase of the strength of the downslope wind which linear steady-state theory would predict. This is precisely the interaction observed in the supercritical $h = 400$ m case described previously.

We are continuing to explore the consequences of the associated wave-mean flow interaction in the context of more realistic atmospheric models. Aside from the obvious extensions of this work to include the effects upon the mechanism of variable stratification and wind shear the character of the flow in the vicinity of the critical level deserves further discussion. Here we have elected to treat the critical layer as dissipative and have used first-order closure to estimate the turbulent diffusion which we *assume* to be associated with convection near the critical level. We are currently conducting experiments in which the nonlinear interaction is completely inviscid and these experiments have demonstrated, as expected (Davis and Peltier, 1977), that the amplification mechanism maintains its efficiency. These experiments will be described elsewhere.

REFERENCES

Acheson, D. J., 1976: On over-reflection. *J. Fluid Mech.*, **77**, 433–472.

Arakawa, A., 1966: Computational design for long term integration of the equations of motion: Two-dimensional incompressible flow. Part 1. *J. Comput. Phys.*, **1**, 119–143.

Batchelor, G. K., 1954: Heat convection and buoyancy effects in fluid. *Quart. J. Roy. Meteor. Soc.*, **80**, 339.

Blumen, W., 1965: A random model of momentum flux by mountain waves. *Geofis. Publ.*, **26**, 1–33.

Booker, J. R., and F. P. Bretherton, 1967: The critical layer for internal gravity waves in a shear flow. *J. Fluid Mech.*, **27**, 513–539.

Breeding, R. J., 1971: A non-linear investigation of critical levels for internal gravity waves. *J. Fluid Mech.*, **50**, 545–563.

Bretherton, F. P., 1969: Momentum transport by gravity waves. *Quart. J. Roy. Meteor. Soc.*, **95**, 213–243.

Clark, T. L., 1977: A small-scale numerical model using a terrain following co-ordinate system. *J. Comput. Phys.*, **24**, 186–215.

Danielson, E. F., and R. Bleck, 1970: Tropospheric and stratospheric ducting of stationary mountain lee waves. *J. Atmos. Sci.*, **27**, 758–772.

Davis, P. A., and W. R. Peltier, 1976: Resonant parallel shear instability in the stably stratified planetary boundary layer. *J. Atmos. Sci.*, **33**, 1287–1300.

——, and ——, 1977: Effects of dissipation upon parallel shear instability near the ground. *J. Atmos. Sci.*, **34**, in press.

Deardorff, W., 1971: On the magnitude of the subgrid-scale eddy coefficient. *J. Comput. Phys.*, **7**, 120–133.

Eliassen, A., and E. Palm, 1960: On the transfer of energy in stationary mountain wave. *Geofis. Publ.*, **22**, 1–23.

Gal-Chen, T., and R. C. Somerville, 1975a: On the use of a coordinate transformation for the solution of the Navier-Stokes equations. *J. Comput. Phys.*, **17**, 209–223.

——, and ——, 1975b: Numerical solution of the Navier-Stokes equations with topography. *J. Comput. Phys.*, **17**, 276–310.

Harlow, F. H., and J. E. Welch, 1965: Numerical calculation of time-dependent viscous incompressible flow of fluid with free surface. *Phys. Fluids*, **8**, 2182–2189.

Howard, L. N., 1961: Note on a paper of John W. Miles. *J. Fluid Mech.*, **10**, 509–512.

Jones, W. L., 1968: Reflexion and stability of waves in stably stratified fluids with shear flow. *J. Fluid Mech.*, **34**, 609–624.

Klemp, J. B., and D. K. Lilly, 1975: The dynamics of wave induced downslope winds. *J. Atmos. Sci.*, **32**, 320–339.

Lapidus, A., 1967: A detached shock calculation by second order finite differences. *J. Comput. Phys.*, **2**, 154–177.

Lilly, D. K., 1962: On the numerical simulation of buoyant convection. *Tellus*, **14**, 148–172.

——, 1967: The representation of small-scale turbulence in numerical simulation experiments. *Proc. IBM Scientific Computing Symposium on Environmental Sciences*, IBM Form No. 320-1951.

——, 1972: Wave momentum flux—a GARP problem. *Bull. Amer. Meteor. Soc.*, **53**, 17–23.

——, and E. J. Zipser, 1972: The front range windstorm of 11 January 1972—a meteorological narrative. *Weatherwise*, **25**, 56–63.

——, and P. J. Kennedy, 1973: Observations of a stationary mountain wave and its associated momentum flux and energy dissipation. *J. Atmos. Sci.*, **30**, 1135–1152.

Long, R. R., 1955: Some aspects of the flow of stratified fluids, III. Continuous density gradient. *Tellus*, **7**, 341–357.

——, 1972: Finite-amplitude disturbances in the flow of inviscid rotating and stratified fluids over obstacles. *Annual Review of Fluid Mechanics*, Vol. 4, Annual Reviews, Inc., 69–92.

Lyra, G., 1943: Theory der stationare Leewellen-Stromung in freier atmosphere. *Z. Angew. Math. Mech.*, **23**, 1–28.

Miles, J. W., 1961: On the stability of heterogeneous shear flow. *J. Fluid Mech.*, **10**, 496–508.

——, 1969: Waves and wave drag in stratified flows. *Proc. 12th Inst. Congress Applied Mechanics*, Hetenyi and Vincenti, Eds., Springer-Verlag, 52–76.

——, and H. E. Huppert, 1969: Lee waves in stratified flow. Part 4. Perturbation approximations. *J. Fluid Mech.*, **35**, 497–525.

Ogura, M., 1969: A direct solution of Poisson's equation by dimension reduction method. *J. Meteor. Soc. Japan*, **47**, 319–323.

Ogura, Y., and N. A. Phillips, 1962: Scale analysis of deep and shallow convection in the atmosphere. *J. Atmos. Sci.*, **19**, 173–179.

Orlanski, I., 1976: A simple boundary condition for unbounded hyperbolic flows. *J. Comput. Phys.*, **21**, 251.

Queney, P., 1941: Ondes de gravite produites dans un courant aerien par une petite chaine de montagnes. *C. R. Acad. Sci. Paris*, **213**, 588.

Sawyer, J. S., 1959: The introduction of the effects of topography into methods of numerical forecasting. *Quart. J. Roy. Meteor. Soc.*, **85**, 31–43.

Schuman, F. G., 1962: Numerical experiments with the primitive equations. *Proc. Int. Symp. on Numerical Weather Prediction*, Tokyo, Meteor. Soc. Japan, 85–107.

Scorer, R. S., 1949: Theory of waves in the lee of mountains. *Quart. J. Roy. Meteor. Soc.*, **76**, 41–56.